ELSEVIER

Assessment of uncertainty in response estimation for turbine engine bladed disks [☆]

Giorgio Calanni Fraccone[a], Massimo Ruzzene[a], Vitali Volovoi[a],[*],
Peter Cento[b], Charles Vining[b]

[a]School of Aerospace Engineering, Georgia Institute of Technology, Atlanta, GA 30318, USA
[b]Arnold Engineering Development Center, Arnold Air Force Base, TN 37389, USA

Abstract

Stress prediction in turbine blades is affected by limitations in the measurement setup as well as by various sources of uncertainty in the model-based inference techniques. The presence of uncertainty diminishes the confidence in the estimated response, whose fidelity lowers further when results are extrapolated to operating conditions or systems other than the tested ones. A procedure is being developed with a twofold objective: maximization, under given computational constraints, of a system's model accuracy and quantification of any remaining uncertainty associated with the estimation technique. A probabilistic analysis, in which uncertainties are explicitly modeled has been carried out to investigate the effects of modeling and input parameter uncertainties, and to evaluate their contribution to a system's vibratory response prediction. Results and considerations are herein described and discussed.
© 2008 Published by Elsevier Ltd.

1. Introduction

Turbine engine tests are conducted to measure the vibratory response of blades or other components under given load conditions, where these measurement data are then used together with a predictive model [1] to infer the critical response levels, and to help in the assessment of a system's fatigue life and reliability. Measurement data are also used to calibrate analytical/numerical models, and to investigate how accurately they can predict a physical system's behavior, which is a major point of interest within the realm of design, as well as for model verification and validation [2]. The accuracy of any response inference technique is limited by a number of factors, concerning the physical system, its structural modeling, and the test setup. On the one hand, sensor-based constraints (e.g., type and number of sensors, measurement inaccuracy, bandwidth, range of operability), validity of measurement data obtained in a controlled test environment (rather than in field conditions), as well as the lack of knowledge of the physical system's true state (e.g., geometric tolerances or

---

unknown boundary conditions) all contribute to the introduction of uncertainty into the measured vibratory response. On the other hand, system models are also affected in their predictive capability by their inherent assumptions and simplifications, whose primary effect is a diminished confidence level associated with the estimation process.

Uncertainties can be broadly grouped into two main categories: physical uncertainties and model-related ones. The first group originates from the difference between a physical system's true state and its model representation, as well as from the discrepancy between actual and nominal testing conditions, while the second stems from the limited fidelity and approximations of the structural model and analysis. Physical uncertainties include, among others, manufacturing variations, sensor calibration and sensitivity, measurement noise, gage nonlinearities, sampling rate and data processing algorithms. On the other hand, modeling uncertainties stem from inexact model geometry and boundary conditions, finite-element discretization level and element formulation, and any other underlying hypotheses feeding into the numerical representation.

Most of the existing literature has focused on geometric and material imperfections and the related phenomenon of blade mistuning [3–6]. The main difficulty in these types of problems lies primarily in two aspects: the random nature of the aforementioned imperfections and the consequent loss of cyclic symmetry due to them, which causes a huge increase in computational costs associated with any probabilistic analysis being performed on full bladed disks. Therefore, together with an appropriate representation of blade mistuning, the other challenge is to develop a reduced-order structural model capable of representing accurately, yet efficiently, the given physical system. Different kinds of reduced-order models have been adopted, using, for instance, component-mode synthesis [7], mean-reduced-matrix models [8], or series of coupled spring-mass-like blades [9,10]. The prediction schemes used for the estimation of the maximum amplitude of a system's forced vibratory response are also quite diversified, ranging from the use of polynomial chaos [10] to the employment of neural networks to establish its functional relationship with the mistuning parameters [11]. Besides addressing geometric uncertainty [3], attention has also been given to the assessment of model-related uncertainties in the presence of measurement errors, in the context of model verification and validation [2]. While mistuning is an important factor within the realm of physical uncertainties, the work presented in this paper is primarily focused on investigating a given model-based response inference process, and on assessing the loss of accuracy due to the various uncertainties inevitably embedded in it. Briefly, such a process consists in estimating the maximum vibratory response of a system via modal scaling of the peak amplitudes observed in test results. Of course, such a technique involves the direct interaction of modeling uncertainty with experiment-related uncertainties. Therefore, the objective of this paper is to quantify the impact of such sources of uncertainty upon the predicted response's accuracy, and to study how experimental uncertainties are propagated through a numerical model, affected by inaccuracies. More specifically, the effects of unknown model characteristics (e.g., mode shape error), sensor measurement and location are explicitly addressed. Despite the fact that several other sources of uncertainty are not directly included in the analysis, their impact could be implicitly taken into consideration by artificially introducing more uncertainty to the sensor data or to the system model. For instance, certain physical uncertainties could be included by introducing a perturbation into the test results in a suitable stochastic fashion. The interaction among uncertainties and their effect on the proposed prediction methodology are first studied on a simple blade model, based on elementary beam theory. The study is then extended to a more realistic blade model, described through a finite-element representation using a commercial package. In both cases, uncertainty is introduced in the form of unknown inputs or perturbation of the model characteristics, where Monte Carlo simulations are the probabilistic analysis tool in use.

The paper is composed of two parts: the first part consists of a description of the inference technique and of the uncertainty sources being herein taken into consideration. The second part presents the uncertainty analysis performed on the beam-like blade and the whole bladed disk.

2. Response estimation methodology

The inference technique adopted in this work consists of scaling the mode shape of the system that best approximates its forced response at the frequency of maximum excitation. In fact, at any point $\mathbf{x} = (x, y, z)$ on the structure, the amplitude $a(\omega, \mathbf{x})$ of the forced harmonic response, at the excitation frequency ω, can be

written as a linear modal expansion:

$$a(\omega, \mathbf{x}) = \sum_{j=1}^{\infty} C_j \phi_j(\mathbf{x}), \qquad (1)$$

where the quantities $\phi_j(\mathbf{x})$ are the structure's mode shapes, and C_j are the coefficients of modal participation, which, in general, may be functions of frequency and/or time. In a case where the excitation frequency ω approaches the natural frequency ω_i of the system, the harmonic response amplitude may be approximated as follows:

$$a(\omega, \mathbf{x}) \approx C_i \phi_i(\mathbf{x}), \qquad (2)$$

where the approximation's accuracy depends on how close ω is to ω_i, and on how distant that mode is, frequency-wise, from its adjacent ones.

When a structure is subject to a harmonic loading condition within a certain frequency range $\Delta\omega$, the mode corresponding to the maximum vibratory response, occurring at the peak frequency $\bar{\omega} \in \Delta\omega$, can be identified through the minimization of a fitness parameter similar to the one defined in [12]:

$$\min_{s,i} \left\{ |\bar{\omega}_s - \omega_i| + \left| \frac{a_1(\bar{\omega}_s)}{a_2(\bar{\omega}_s)} - \frac{\phi_i(\mathbf{x}_1)}{\phi_i(\mathbf{x}_2)} \right| \right\}, \quad i = 1, 2, \ldots, \tau, \ s = 1, 2, \qquad (3)$$

where $\bar{\omega}_s$ and $a_s(\omega)$ are, respectively, the peak frequency and the amplitude of the forced harmonic response recorded by the s-th sensor at its location $\mathbf{x}_s$ ($s = 1, 2$) on the component. The quantities ω_i and $\phi_i(\mathbf{x})$ are obtained by means of the component's structural model, with τ representing the number of mode shapes considered in the analysis. The minimization on s is performed to account for those situations in which the peak frequencies measured by the sensors differ from one another due, for instance, to measurement errors. The considerations made throughout this work refer to the particular case where a given component is assumed to be instrumented with only two sensors. This does not represent a loss of generality since an extension to a larger number of gages is straightforward and does not add further insight to the discussion. In addition, it is worth noting that the response inference technique is independent of the nature of the estimated response which, in turn, is a function of the type of sensors being used (e.g., strain gages, displacement sensors, or other). As a consequence of that, the proper modal quantities are to be utilized within Eqs. (3) and (4).

Given the best fitting mode(s) ϕ_{h_s} ($1 \leqslant h_s \leqslant \tau$) as identified via Eq. (3), the maximum amplitude of the vibratory response $a^{(\max)}$ can be extrapolated by weighing the information measured by the two sensors:

$$a^{(\max)} = \max_{s=1,2} \left\{ \max \left\{ a_1(\bar{\omega}_s) \frac{\bar{\phi}_{h_s}}{\phi_{h_s}(\mathbf{x}_1)}, a_2(\bar{\omega}_s) \frac{\bar{\phi}_{h_s}}{\phi_{h_s}(\mathbf{x}_2)} \right\} \right\}, \qquad (4)$$

where $\bar{\phi}_{h_s} = \max_{\mathbf{x}} \phi_{h_s}(\mathbf{x})$ is the maximum of the h_s-th mode. The two quantities within parentheses are usually expected to be rather similar in values. This is not the case if the sensors record different peak frequencies causing different modes to be selected through Eq. (3). As a consequence of that, $a^{(\max)}$ could also be inferred by averaging the estimates rather than selecting the maximum value, as that could overestimate the actual maximum response. Eq. (4) is herein used as the basis for the analysis of various sources of uncertainty and of their impact on stress estimation. The value of the inference technique has been investigated for two different types of systems, a beam-like blade and a turbine engine rotor.

3. Sources of uncertainty

The types of uncertainties being considered in this study include input uncertainties, sensor-based, and modeling ones. The first type is associated with the limited knowledge of system dimensions (for example, due to tolerances) and material characteristics. The second and third kind are introduced, respectively, to account for several sources of uncertainty due to out-of-control experimental conditions and/or instrumentation limitations (e.g., measurement inaccuracy, sensor sensitivity to external conditions), and to study the effect of a discrepancy between the physical system and the analytical (or numerical) model.

3.1. Input uncertainty

Uncertainty on a physical system's material characteristics (e.g., Young's modulus or density) and dimensions due, for instance, to manufacturing imprecision and machine tolerances can cause the "true" (but unknown) inputs to the model to deviate from the "nominal" values (i.e. used in the model), thus resulting in the difference in response between the actual system and the model prediction.

3.2. Sensor-based uncertainties

The estimation of a system's maximum response also is affected both by uncertainty in the amplitudes read by the sensor, and by limited knowledge of its exact placement. Uncertainty on a sensor's reading can be caused by several factors, which include, among others, measurement noise, nonlinearity of response, and/or a strain gage's imperfection in the adhesion to the component. The impact of a sensor measurement error on the response estimation has been investigated by perturbing the sensed amplitude $a_s(\omega)$ by a random quantity ε_s. More specifically, the following formulation has been adopted:

$$\hat{a}_s(\omega) = a_s(\omega) + A\varepsilon_s,$$
$$\varepsilon_s = N(0, \sigma_s^2), \quad s = 1, 2, \tag{5}$$

where $\hat{a}_s$ defines the perturbation of the sensed vibratory amplitude with respect to the nominal value a_s, and ε_s has been assumed to be normally distributed with zero mean and standard deviation σ_s. Uncertainty is introduced through a sensor's noise parameter A defined herein as a percentage of the maximum response amplitude for the mode identified by the estimation process (Eq. (3)). This definition is an attempt to account for uncertainty in the sensor measurements, while removing, at the same time, the dependence of A upon the sensor's reading and, indirectly, position on the component. In fact, in a test, sensors of the same type, placed at different locations, may be subject to quite different conditions (e.g., pressure, temperature, or loads) which may significantly affect their accuracy across the same measurement range. At present, no specific type of sensor (e.g., NSMS, strain gage or accelerometers) has been taken into consideration. However, a more rigorous definition for ε_s may be needed when considering a given sensor type so as to account for its specific characteristics and gain better and more realistic insight.

Uncertainty associated with sensor location can be introduced in a similar fashion, i.e. by perturbing the modal information at the gages' position before using it in Eq. (4):

$$\hat{\phi}_{h_s}(\mathbf{x}_s) = \phi_{h_s}(\mathbf{x}_s + \zeta_s), \quad s = 1, 2, \tag{6}$$

where ζ_s represents the difference between nominal and actual position of the sensor on the system. Since the real sensor's location is uncertain, ζ_s is treated as a random quantity, which, however, still need satisfy given geometry constraints (e.g., surface contact between strain gage and component). Given the geometry-dependent nature of this approach, more detailed discussions are provided in subsequent sections where specific geometric configurations have been addressed.

3.3. Modeling uncertainty

Another source of uncertainty which may affect the effectiveness of the inference process is represented by the limited accuracy of the system model at hand. Among the several factors influencing model inaccuracy, attention is given to the effect of a mismatch between experimental and numerical mode shapes used to perform the estimation. Such a discrepancy is reproduced by perturbing the model mode shapes so as to simulate those circumstances in which the model is not capable of capturing entirely the behavior of the tested unit. Given the experimental mode shape $\phi_i^{(e)}$ and the corresponding model mode shape $\phi_i^{(m)}$ ($i = 1, 2, \ldots, \tau$), the mismatch between the two has been introduced as follows:

$$\phi_i^{(e)} = \sum_{j=-1}^{1} w_{i-j} \phi_{i-j}^{(m)}. \tag{7}$$

In this case, the experimental mode $\phi_i^{(e)}$ is expressed as a linear combination of the i-th mode shape and its frequency-wise immediate neighbors, through the set of weights (w_{i-1}, w_i, w_{i+1}). The correlation between experimental and model modes (or between perturbed and unperturbed modes in the case of computer simulated experiments) can be established through the Modal Assurance Criterion (MAC) [13]:

$$\mathrm{MAC}_{p,q} = \frac{|\phi_p^{(e)^\mathrm{T}} \phi_q^{(m)}|^2}{|\phi_p^{(e)^\mathrm{T}} \phi_p^{(e)}||\phi_q^{(m)^\mathrm{T}} \phi_q^{(m)}|}, \quad p, q = 1, 2, \ldots, \tau. \tag{8}$$

The MAC matrix is close to an identity matrix when good correlation exists between the two sets of mode shapes. In this particular setting of simulated experiments, it also offers a way to quantify the amount of perturbation introduced by a given set of weights.

4. Uncertainty analysis on a beam-like blade model

4.1. Configuration and modeling assumptions

The beam-like blade being considered in this study is part of the simplified rotor model shown in Fig. 1. Despite its simplicity, the model accounts for blade-to-blade coupling and for rotor flexibility via concentrated spring elements, as well as centrifugal stiffening of the blades due to their precession about the shaft axis [14]. More realistic boundary conditions, such as blade attachments and pressure loads, were not taken into account here, but would need to be included in more advanced models. Stresses and displacements in the blades are computed for assigned inputs and loading conditions (i.e. amplitude, excitation frequency ω, and point of application along the blade), engine operating condition (i.e. the angular velocity Ω), as well as the blade geometry and material characteristics (Table 1). It is standard practice to synthesize stresses and displacements in the form of Campbell diagrams, which summarize the response amplitudes over the considered range of frequencies and rotor speeds [15]. The Campbell diagram is used to identify the so-called
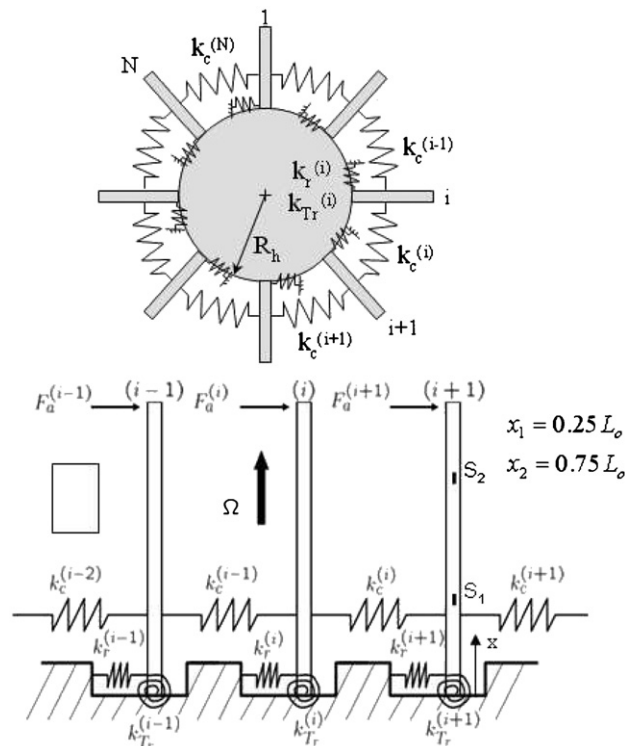

Fig. 1. Schematic of a simplified model of a bladed disk.

Table 1
Beam geometry and properties

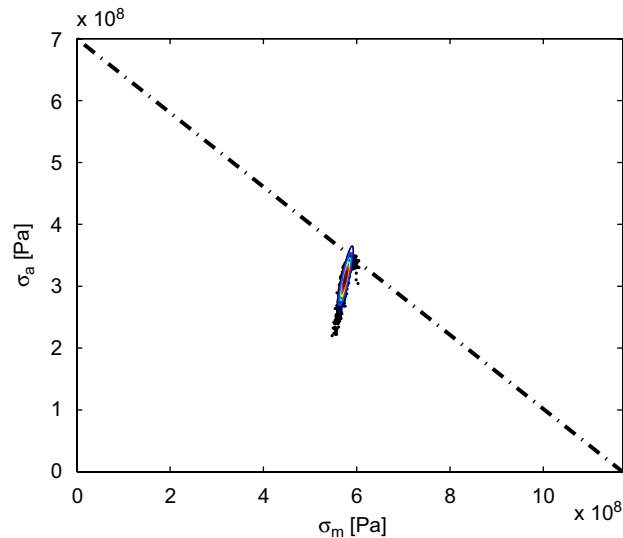| Quantity	Symbol	Value
Length	L_0	22.5 cm
Thickness	t_0	2 cm
Chord	c_0	15.3 cm
Density	ρ_0	4430 kg/m^3
Young's modulus	E_0	114 GPa

Fig. 2. Goodman diagram for a single blade: —·— fatigue limit.

"resonant blossoms" of a rotating system, i.e. regions with high stress levels corresponding to blade resonance due to the intersection of an engine order excitation with one of the blade's natural frequencies. A system's maximum vibratory response obtained from the Campbell diagram can then be combined with its static response in a Goodman diagram to assess the risk of fatigue failure.

4.2. Input uncertainty

The effect of an input uncertainty propagation is addressed through a sensitivity study on the Goodman diagram, where variations both in geometry (i.e. length L_0, cross dimensions t_0, and c_0) and material properties (i.e. E_0 and ρ_0) have been evaluated using the system model described in the previous section. For this particular system, a point Σ on the Goodman diagram is identified as

$$\Sigma = (\sigma_a^{(\max)}, \sigma_m), \tag{9}$$

where the maximum longitudinal alternating stress $\sigma_a^{(\max)}$ on the blade is herein defined as

$$\sigma_a^{(\max)} = \max_{\Omega,\omega}\left(\max_x |\sigma_a(x)|\right), \tag{10}$$

so as to account for both the operating condition and the excitation frequency of the forcing function. The mean stress σ_m corresponds, instead, to an equivalent mean load statically applied at the blade's tip. As an example, illustrated in Fig. 2 is the effect of a 2% variation in chord and thickness, where the perturbations have been assumed to have a normal distribution. As can be observed from the plot, some combinations of

beam section dimensions may cause the structure to be significantly close to its fatigue limit or to exceed it. A sensitivity study on beam length produced a similar spread of the stress levels, whereas no significant scatter in the response was observed when varying the material properties.

4.3. Sensor-related uncertainty

Uncertainty in sensors' readings and locations have been investigated via 10,000-sample Monte Carlo simulations. The effect of a sensor measurement error upon the estimate of a system's response has been introduced according to Eq. (5) with the assumption that $\sigma_{s=1,2} = \sigma = 0.01$. Furthermore, taking into account the one-dimensional nature of the beam analysis, uncertainty in the location of the s-th sensor is expressed by means of Eq. (6) with the nominal position x_s, along the span, being perturbed in the following manner:

$$\hat{x}_s = x_s + \frac{L_r}{2} N(0, \sigma^2), \quad s = 1, 2, \tag{11}$$

where the perturbed location $\hat{x}_s$ is computed in terms of a reference length L_r which denotes the blade span L_0.

In this study, uncertainties in sensor measurement and position have been addressed separately. Despite the fact that this distinction may be somewhat hard to make in real test conditions, it still offers valuable insight with respect to uncertainty propagation. The effect of each source of uncertainty has been investigated and quantified through 10,000-run Monte Carlo simulations, where a nondimensional variance σ^2 of 0.01^2 has been assumed for all case studies. Furthermore, results are presented in the form of a variability of an absolute error, defined as the difference between the estimates obtained from the inference process and the actual response resulting from a forced harmonic analysis conducted on the system model.

Shown in Figs. 3 and 4 is the variability in displacement and stress estimates due to uncertainty in sensor positions. Each plot compares the uncertainty resulting from the perturbation of each sensor separately. Of course, this one-at-a-time approach is an idealization, whereas a larger uncertainty may result from both sensors being in nonnominal conditions at the same time, which could affect the mode identification process through the ratio $\phi(\mathbf{x}_1)/\phi(\mathbf{x}_2)$, as well as the accuracy of the estimates due to the coupling between the perturbed sensor position $\hat{x}_s$ and the amplitude of the selected mode $\phi_{h_s}(x)$ at that location. Illustrated in Fig. 5 is the case in which both sensors' positions have been randomly varied simultaneously. In this circumstance, the estimates' variability appears to be skewed. This behavior, however, has no physical basis, but it is merely due to the discrete nature of Eq. (4), where one estimate was probabilistically higher than the others, hence prevailing in the maximization process. When treated individually, each estimate exhibited a
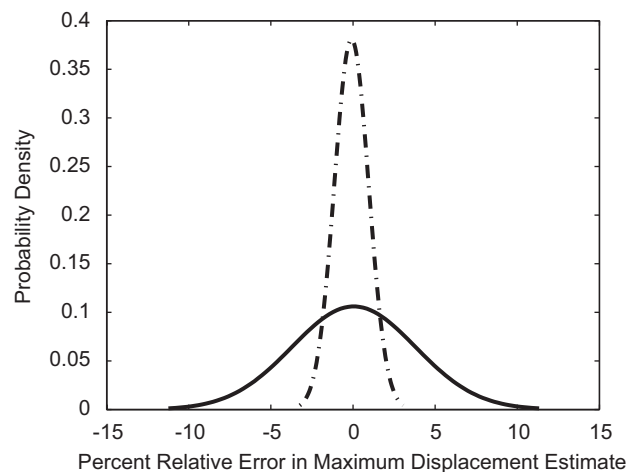

Fig. 3. Variability in maximum-displacement estimate due to uncertainty in sensor location ($\sigma = 0.01$): $-S_1$; and $-\cdot- S_2$.
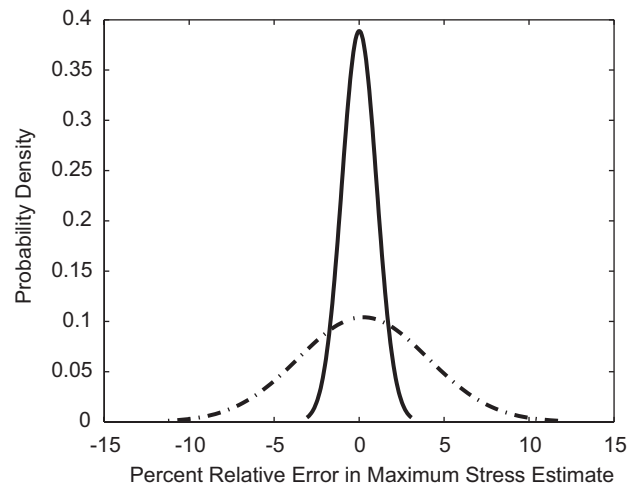
Fig. 4. Variability in maximum-stress estimate due to uncertainty in sensor location ($\sigma = 0.01$): S_1; and $-\cdot-$ S_2.
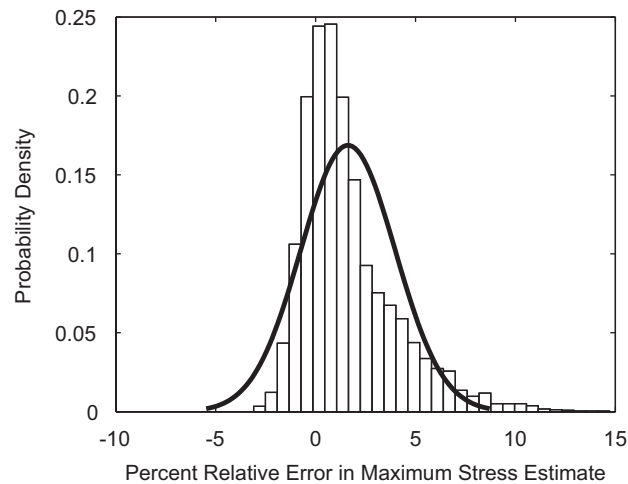

Fig. 5. Variability in maximum-stress estimate due to uncertainty in both sensor locations ($\sigma = 0.01$): $\square$ histogram of combined estimates at sensors S_1 and S_2; and — approximating Gaussian distribution.

normally distributed trend similar to the one of Figs. 3 and 4. Overall, despite their limited validity due to the simple nature of the system and the sensor's point representation, these results highlight how the variability in stress and displacement estimates depends significantly upon the location where measurements are taken, thus suggesting the need for optimal placement of the instruments together with a better and more accurate description of their characteristics [16,17].

The effect of an uncertainty in sensor readings is illustrated in Fig. 6. The results shown were obtained by varying only one measurement data set at a time, while assuming a 100% accuracy for the other sensor. Similarly to what was observed when varying the sensor locations, the results show that the response estimates are characterized by a different variability for each of the sensors, which could be related to the difference in the signal-to-noise ratio at the various instrument locations. Therefore, this behavior suggests that the effect of a measurement uncertainty could also depend upon sensor placement, thus making any distinction between the two sources of uncertainty more difficult to draw. Finally, when both sensors' measurements were varied simultaneously, results similar to the ones depicted in Fig. 6 were observed. This is exclusively due to the fact
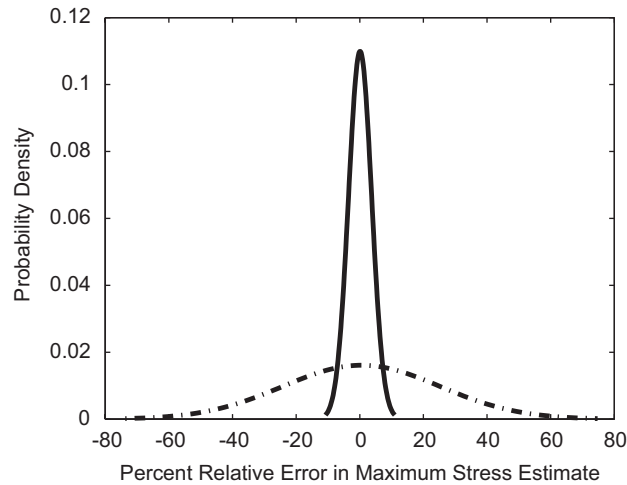
Fig. 6. Variability in maximum-stress estimate due to uncertainty in sensor reading ($\sigma = 0.01$): — S_1; and $-\cdot-$ S_2.

that the estimates in Eq. (4) are only coupled through ϕ_{h_s}, and the same mode shape was always selected regardless of whether only one or both sensor readings were being perturbed.

4.4. Modeling uncertainty

In order to study the effect of modeling uncertainty for the beam-like blade system, two sets of weights were used in Eq. (7) to perturb its mode shapes, each of which represented a model of different accuracy. The two system models were compared by means of their MAC matrices, according to which configuration 2 indicates a better correlation between perturbed and unperturbed quantities (Fig. 7). The modal assurance criterion represents a common and widely accepted means to assess the degree of correlation between perturbed and unperturbed modes, or between a physical system and its analytical representation. In order to evaluate the effect of modeling uncertainty on the prediction of a system's response, the perturbed modes $\phi^{(e)}(x)$ were used in conjunction with a random variation in the sensor locations:

$$\hat{\phi}_i^{(e)}(x_s) = \phi_i^{(e)}(x_s + \zeta_s), \quad i = 1, \ldots, \tau,$$
$$\zeta_s = N(0, \sigma_s^2), \quad s = 1, 2, \tag{12}$$

where the Gaussian quantity ζ_s represents the variability associated with the s-th sensor position. Depicted in Fig. 8 is the result of a Monte Carlo simulation with $\sigma_{s=1,2} = \sigma = 0.01$. The beam was assumed to be instrumented with only one strain gage and the response estimates were obtained by plugging Eq. (12) into Eq. (4). As shown in Fig. 8, configuration 2 indicates a likelihood of less variability in the maximum-stress estimation, thus demonstrating for this simple model that a lower modeling uncertainty yields a higher prediction confidence, and that any additional variability should be ascribed to input parameter uncertainty.

5. Uncertainty analysis on a bladed disk model

The same analysis process illustrated earlier has also been employed to estimate the critical vibratory response of a compressor rotor disk representative of the system treated in Ref. [18], whose characteristics are listed in Table 2. Due to the lack of experimental data, harmonic analyses with various cyclic loading conditions have been conducted on a finite-element model to simulate different testing conditions. The data were then used together with modal information to assess the goodness of the inference
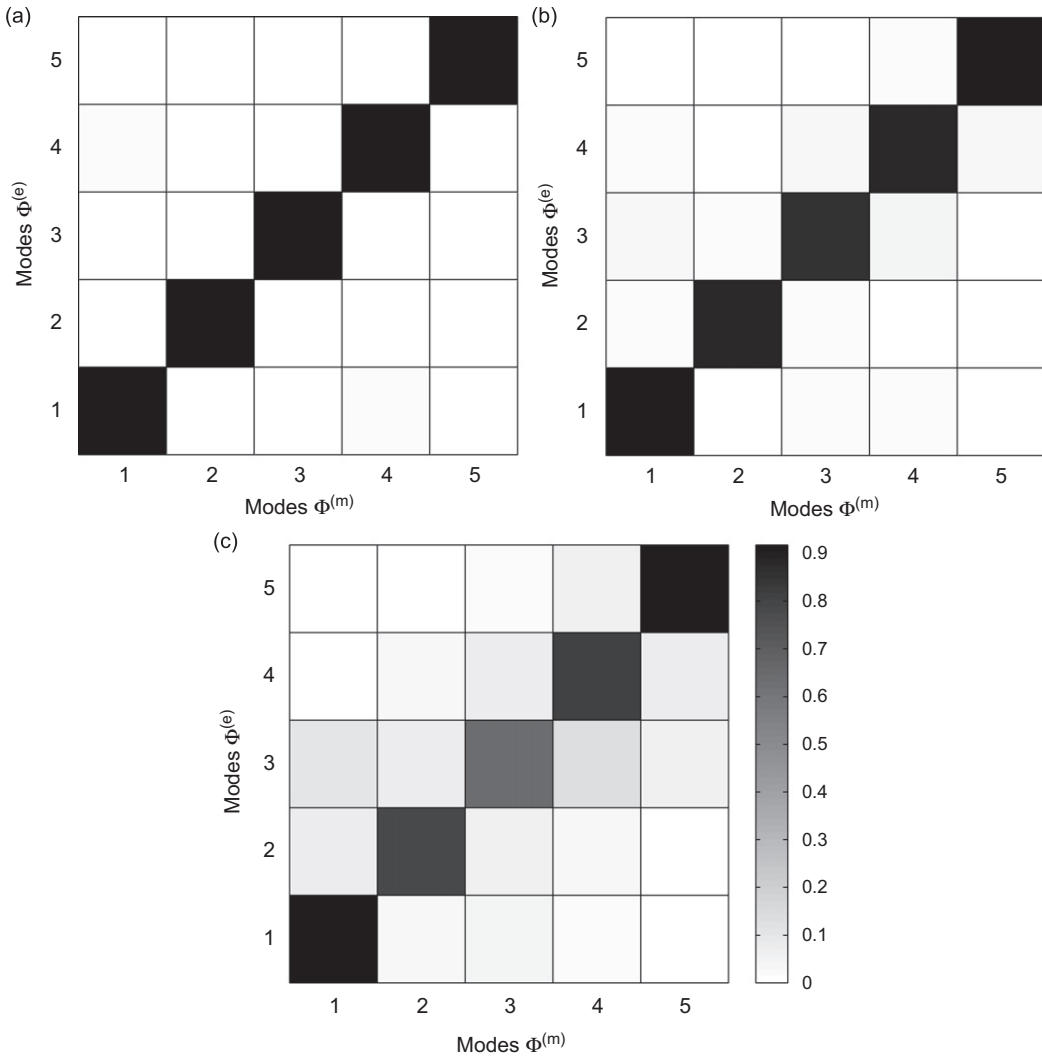
Fig. 7. MAC configurations ($\tau = 5$): (a) configuration 1 ($w_{-1} = 0$, $w_0 = 1$, $w_1 = 0$); (b) configuration 2 ($w_{-1} = 0.1$, $w_0 = 0.8$, $w_1 = 0.1$); and (c) configuration 3 ($w_{-1} = 0.15$, $w_0 = 0.7$, $w_1 = 0.15$).

process as well as to address the propagation of input and modeling uncertainty through Monte Carlo simulations.

5.1. Configuration and modeling assumptions

The disk is composed of nineteen nominally identical sectors. A single sector is modeled in the commercial finite-element package ANSYS©, using the mesh depicted in Fig. 9. The model is discretized using SOLID95 elements, where blades and disk are considered as a single integral unit. Zero-displacement conditions are imposed at the disk-shaft interface. The structure's cyclic nature is taken into account by imposing compatibility constraints in the form of a set of periodic boundary conditions on the sector sides, similar to the ones discussed in Refs. [19,20]. Using the duplicate-sector approach, such boundary conditions can be expressed as follows:

$$
\left\{ \begin{array}{c} U_B \\ U_D \end{array} \right\}_{\text{side 2}} = \left[\begin{array}{cc} \cos k\alpha & \sin k\alpha \\ -\sin k\alpha & \cos k\alpha \end{array} \right] \left\{ \begin{array}{c} U_B \\ U_D \end{array} \right\}_{\text{side 1}},
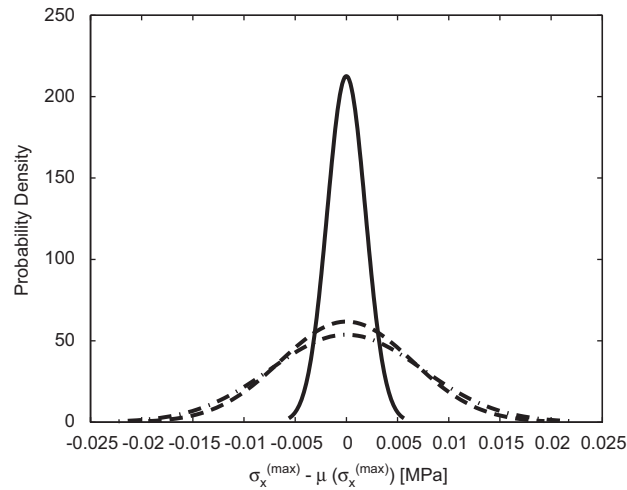\tag{13}
$$

Fig. 8. Variability in maximum-stress estimate due to nonunitary MAC matrices: — MAC configuration 1; – – MAC configuration 2; and —·— MAC configuration 3.

Table 2
Disk characteristics

Quantity	Symbol	Value
Blade height	h_b	5.08 cm
Blade chord	c_b	12.7 cm
Disk outer radius	R_h	10.16 cm
Shaft radius	R_s	1.27 cm
Disk thickness	t_d	1.52 cm
Material		Ti-6-4
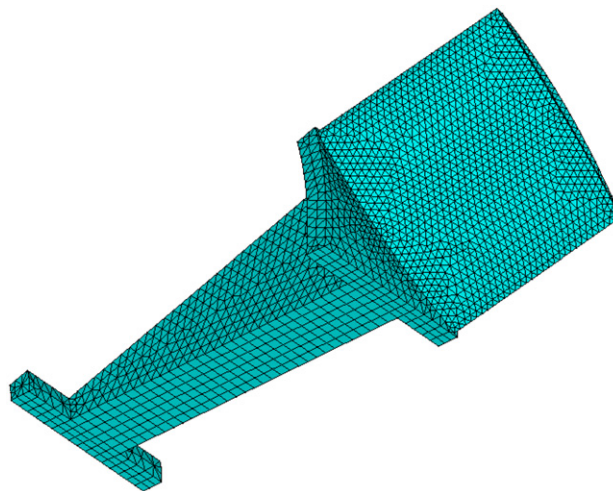
Fig. 9. Finite element model of a disk sector.

where B and D represent the basic sector and its duplicate, respectively, with one exactly overlapped onto the other. Eq. (13) establishes a constraint, for each cylindrical degree of freedom U (i.e. displacements and rotations), between the nodes on the sides of the two sectors, where $\alpha = 360°/N$ is the sector angle and where

the harmonic index k is defined as

$$k = \begin{cases} 0, 1, \ldots, \dfrac{N}{2}, & N \text{ even}, \\ 0, 1, \ldots, \dfrac{N-1}{2}, & N \text{ odd}. \end{cases} \quad (14)$$

Given an external load applied on the j-th sector, a Fourier transformation process is used to convert it into an equivalent set of loads applied on the basic and duplicate sectors, whose displacement fields $[(U_B)_k, (U_D)_k]$ are computed individually for each value of the harmonic index. The displacement field for the entire structure is obtained via superposition of the single contributions [21]:

$$U_j = \sum_{k=0}^{\max(k)} (U_B)_k \cos[(j-1)k\alpha] - (U_D)_k \sin[(j-1)k\alpha], \quad j = 1, \ldots, N, \quad (15)$$

where, of course, the same relationship also holds for the stress field.

In order to excite the cyclic structure at a natural frequency $\omega_{n,k}$, a forcing function $\mathbf{F}$ of the following form is to be applied on the disk sectors:

$$\mathbf{F}_j = \mathbf{F}_0 e^{[\omega t + 2\pi k((j-1)/N) + (2\pi/N)\delta]}, \quad j = 1, \ldots, N, \quad (16)$$

where $\mathbf{F}_0$ is the force amplitude, ω is the excitation frequency, and the integer δ accounts for the arbitrariness that is still available phase-wise after the coordinate system is assigned on the model in conjunction with the arbitrary numbering of the sectors. The effect associated with such an angular shift is a rigid rotation of the forced-response deformation by an amount δ, which represents an extra degree of freedom within the response estimation procedure. A similar arbitrariness also appears in the modal analysis, where two modes associated with the same natural frequency $\omega_{n,k}$ can exist. The relationship between two such modes, $\phi_{n,k}^{(1)}$ and $\phi_{n,k}^{(2)}$, is given by

$$\phi_{n,k}^{(1)} = \phi_{n,k}^{(2)} e^{i(2\pi/N)\theta}, \quad \theta = \text{arbitrary integer}, \quad (17)$$

where, in general, $\theta \neq \delta$.

In a case where a double-mode frequency is excited, it is necessary to account for the angular shift between the repeated modes and the forced deformation itself, before the maximum vibratory response can be estimated via modal scaling. In such a case, the forced response at a frequency $\bar{\omega}$ near the natural frequency $\omega_{\bar{n},\bar{k}}$ can be approximated, at any point $\mathbf{x}$ in the structure, as

$$a(\bar{\omega}, \mathbf{x}) = \alpha \phi_{\bar{n},\bar{k}}^{(1)}(\mathbf{x}) + \beta \phi_{\bar{n},\bar{k}}^{(2)}(\mathbf{x}), \quad (\alpha, \beta) \in (\Re, \Re). \quad (18)$$

The sensor measurements (a_1, a_2) can be used to compute the coefficients α and β:

$$\begin{Bmatrix} \bar{\alpha} \\ \bar{\beta} \end{Bmatrix} = \begin{bmatrix} \phi_{\bar{n},\bar{k}}^{(1)}(\mathbf{x}_1) & \phi_{\bar{n},\bar{k}}^{(2)}(\mathbf{x}_1) \\ \phi_{\bar{n},\bar{k}}^{(1)}(\mathbf{x}_2) & \phi_{\bar{n},\bar{k}}^{(2)}(\mathbf{x}_2) \end{bmatrix}^{-1} \begin{Bmatrix} a_1(\bar{\omega}) \\ a_2(\bar{\omega}) \end{Bmatrix}. \quad (19)$$

The two sensors are not to be placed on the same sector so as not to have a redundant set of equations. Finally, only a single estimate for the maximum vibratory condition can be obtained through maximization of Eq. (18):

$$a^{(\max)} = \max_{\mathbf{x}} \| \bar{\alpha} \phi_{\bar{n},\bar{k}}^{(1)}(\mathbf{x}) + \bar{\beta} \phi_{\bar{n},\bar{k}}^{(2)}(\mathbf{x}) \|, \quad (20)$$

which, in the special case of double modes, ought to replace Eq. (4) within the response inference process.

5.2. Results

In this study, measurement data was simulated by means of harmonic analyses, conducted over different ranges of the excitation frequency, for which periodic loads of the form given by Eq. (16) were applied on the

Table 3
Disk natural frequencies (Hz)

Mode no.	Harmonic Index			
	0	1	2	3
1	1071.9	839.37	1190.1	1414.5
2	1231.4	839.37	1190.1	1414.5
3	1946.1	1609	1846.4	3085.1
4	3378.4	1609	1846.4	3085.1
5	5434.6	3374.4	3390.6	3499.8
6	6977.6	3374.4	3390.6	3499.8
Mode no.	4	5	6	7
1	1441.6	1449.2	1452.1	1453.2
2	1441.6	1449.2	1452.1	1453.2
3	3346.2	3361.3	3366.4	3368.9
4	3346.2	3361.3	3366.4	3368.9
5	4554.3	5428.7	5987.5	6333.4
6	4554.3	5428.7	5987.5	6333.4
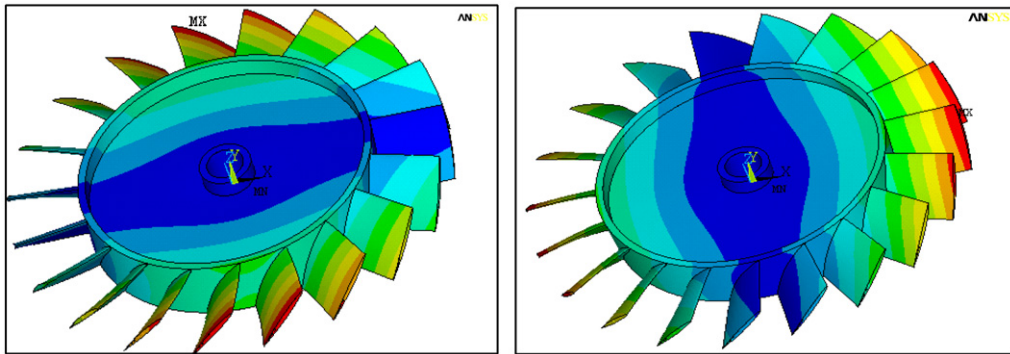
Fig. 10. Double modes of the bladed disk at $\omega = 839.37\,\text{Hz}$.

blades' tips in radial or transverse direction. Two sensors, S_1 and S_2, were considered at locations on the span-wise upper part of the blade, one on the pressure surface and the other on the suction surface of two distinct blades, four sectors apart. The other set of information needed for the estimation of the forced response is obtained through modal analysis. Listed in Table 3 are the structure's natural frequencies obtained through the finite-element model, while depicted in Fig. 10 is one of its double mode shapes.

The following presents some case studies which illustrate the effects of sensor-related uncertainties, modeling accuracy as well as their combined impact and propagation.

5.2.1. Sensor measurement error and location uncertainty

Measurement errors are herein introduced according to Eq. (5) described in Section 3.2, where the perturbation to the nominal measurements is assumed to be normally distributed with standard deviation $\sigma = 0.01$ and gage noise A equal for all the sensors. Shown in Fig. 11 is the result of a Monte Carlo simulation in which only the readings of sensor S_1 were assumed to be affected by uncertainty. As it can be observed, the interpolated probability distribution fits well the simulation histogram data. Depicted in Figs. 12 and 13, instead, is a comparison between the probability density functions of the two estimates, with sensor measurements perturbed separately. In Fig. 12, the estimate's relative error on stress due only to a reading uncertainty in sensor S_2 is characterized by a smaller spread when compared with the estimate's variability
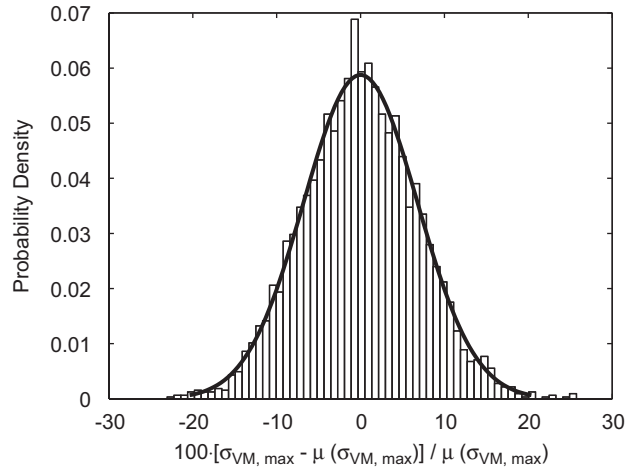
Fig. 11. Variability in maximum-stress estimate due to reading uncertainty in sensor S_1 ($\omega_{1,0} = 1071.9$ Hz): □ histogram of estimate at sensor S_1; and — approximating Gaussian distribution.

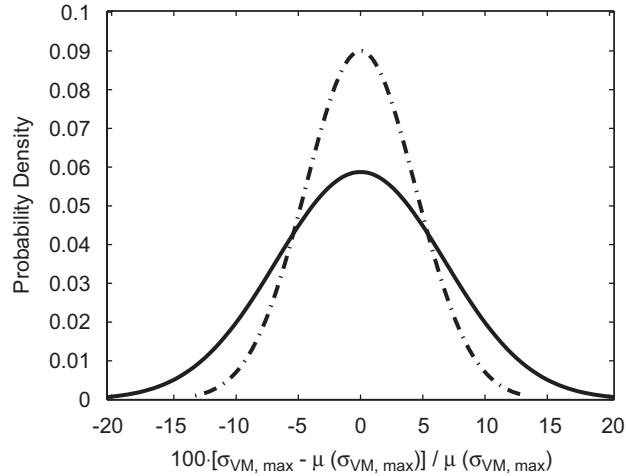Fig. 12. Sensor-based comparison of variabilities in maximum-stress estimate ($\omega_{1,0} = 1071.9$ Hz): — S_1; and $-\cdot-$ S_2.

associated only with a measurement error in the other sensor. An opposite result can, instead, be observed in Fig. 13. Of course, in the particular case of a double mode being excited, both sensor readings do play a role in the estimation process via Eq. (19), thus making it difficult to assess their relative impact on the resulting uncertainty. Furthermore, the sensor positioning also comes into play through the values of the modal quantities at the given locations, which could reduce or amplify a given uncertainty. Finally, shown in Fig. 13 is also the effect of both sensor readings being varied at the same time, for which case the overall spread of the estimated forced response seems to worsen, as it should be expected.

Uncertainty in sensor location is introduced by replacing the modal information corresponding to sensor nominal locations with modal values associated with their perturbed positions. In this instance, however, sensors were placed on the suction and/or pressure surfaces of the blade for which no analytical formulation was available, thus requiring numerical interpolation. The nominal position of a sensor, (x_0, y_0, z_0), is such that

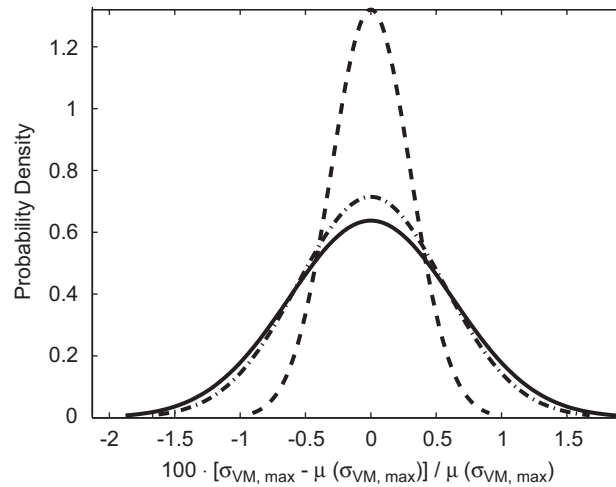$$z_0 = g(x_0, y_0), \tag{21}$$

Fig. 13. Sensor-based comparison of variabilities in maximum-stress estimate ($\omega_{3,6} = \omega_{4,6} = 3366.4$ Hz): — S_1&S_2; – – S_1; and –·– S_2.

where $g(x, y)$ represents the equation of the blade's suction or pressure surface in the xy plane perpendicular to the disk rotational axis. The suction and pressure surfaces are treated separately simply to have a well-posed problem, since g^{-1} cannot otherwise be defined univocally. Obviously, any perturbed position $(\hat{x}_0, \hat{y}_0, \hat{z}_0)$ needs also satisfy such a constraint to guarantee full contact between blade and sensor as well as to preserve the condition of no penetration. That is achieved by computing $\hat{z}_0 = g(\hat{x}_0, \hat{y}_0)$ via linear interpolation over the surface finite-element mesh. The uncertainty on sensor locations has been implemented by generating a statistical realization around the projection onto the xy plane of each sensor's position, and by computing the corresponding modal information to be used within the estimation process. In order to avoid the results being artificially skewed due to the orientation of the blade with respect to the xy plane, the two-dimensional and normally-distributed realization is generated to be bounded by the projection of a circle of radius L_r centered at (x_0, y_0, z_0) and tangent to the blade. In mathematical terms, in a coordinate system $x'y'$ centered and aligned with the projected ellipse's axes, the realization can be written as follows:

$$\hat{x}_0' = N(0, r_{x'}/3),$$

$$\hat{y}_0' = N(0, r_{y'}/3), \tag{22}$$

where $r_{x'}$ and $r_{y'}$ are the measures of the ellipse's semi-axes, and a 3σ limit has been utilized. Such a technique has been employed because of its simplicity as well as its capability to control the statistical realization so that it covers the area around a sensor's nominal position in a more regular fashion, without introducing extraneous sources of asymmetry in the estimates. A study on the impact of sensor location's uncertainty upon the accuracy of the estimation technique was performed through Monte Carlo simulations where both sensors were perturbed, according to Eq. (22), with a reference radius $L_r = .15$ cm. A sample of the results is given in Fig. 14. Illustrated in the figure are the histogram of the relative error of the stress estimate associated with sensor S_2, and its representative probability density function, constructed under the assumption that the sample data are part of a normally distributed population. The formulated assumption is, however, somewhat in contradiction with the skewness shown by the bar chart. The primary cause of such a behavior is twofold: on the one hand, the modal quantities being perturbed (and interpolated upon) appear in the denominator of Eq. (4), which causes the scaling modal ratios to no longer have a normal distribution; on the other hand, the estimates' distributions are a one-dimensional synthesis of at least a two-dimensional spatial uncertainty, whose effect depends on the modal shapes and is furthermore filtered by the interpolation scheme. As a matter of fact, it was furthermore observed that if the sensor's nominal position falls in the vicinity of a maximum or minimum of the excited mode shape, the estimates' histograms become even more skewed, thus making the assumption of normality less appropriate, and the estimation itself less meaningful.
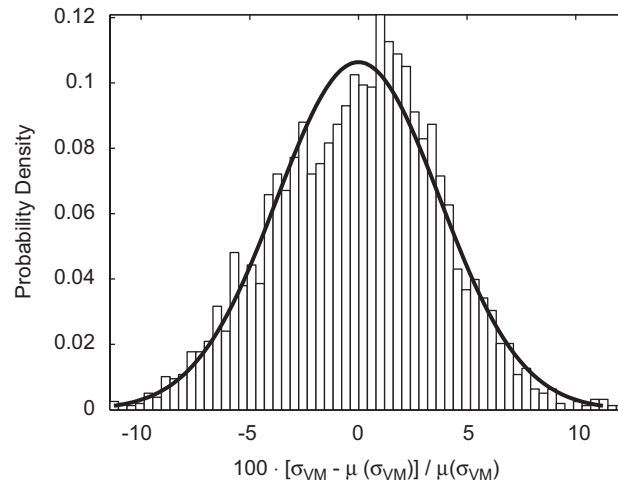
Fig. 14. Variability in maximum-stress estimate due to uncertainty in sensor locations ($\omega_{1,0} = 1071.9$ Hz): □ histogram of stress estimate at sensor S_2; and — approximating Gaussian distribution.

Moreover, according to Eq. (6), the impact of sensor placement uncertainty could be quantified in terms of modal gradients at the nominal gage locations. In fact, the larger the gradient is, the more a location error is expected to be amplified within the estimated response's variability, thus providing a first-order figure of merit for assessing its effect.

A sensitivity study was also conducted where nine different nominal positions for each sensor were considered and perturbed as previously described. The sensors were placed one on each blade surface, where three different nominal positions were considered chord-wise at three locations along the span. Depicted in Figs. 15 and 16 are the nominal positions and realizations on the pressure surface for sensor S_1, and the corresponding uncertainty levels in the response prediction. Simply for the sake of clarity, only five of the nine probability curves are shown, and no histogram associated with those distributions has been displayed. As observed also for the beam case, results show a dependence of the response estimate's accuracy upon a sensor location, with the relative error ranging from 5% up to 15% in this particular case. Of course, this raises the issue of optimal positioning of the instrumentation to achieve better accuracy. It can be rather difficult to draw a clear-cut conclusion on where to place a sensor so as to minimize the error in the inference process, as several factors may come into play, such as magnitudes of the modal quantities near the sensor locations, and gradients which may not be known a priori, until more information is available about the external forcing function or on which mode will presumably be excited. Regions of very low magnitude or strong gradients give rise to very large spreads in the estimates, whereas the estimation process fails when a sensor is placed rather close to a node of the given selected mode. Predicting the sensors' optimal positions can become even harder when double modes are excited, as the way they superimpose depends inherently on the sensor information (Eq. (19)) and locations which are being optimized for. On the other hand, modal ratios at the sensor positions could provide initial insight in the case of single modes.

5.2.2. Modeling uncertainty

As previously exemplified for the beam-like blade, uncertainty in the finite-element model of the disk is introduced by perturbing the model mode shapes according to Eq. (7) and by using the modified quantities within the inference procedure. Shown in Fig. 17 are three MAC configurations, each of which represents a different level of perturbation of the model modes. The combined effect of sensor reading error and modeling uncertainty is depicted in Figs. 18 and 19, where the double-mode frequency 839.37 Hz has been excited, and the only difference between the two graphs is in the different normalization scheme used for the estimate. In this circumstance, according to Fig. 18, different MAC configurations result in very similar spreads of the relative error of stress estimate, while Fig. 19 shows how a higher modal perturbation results in higher bias
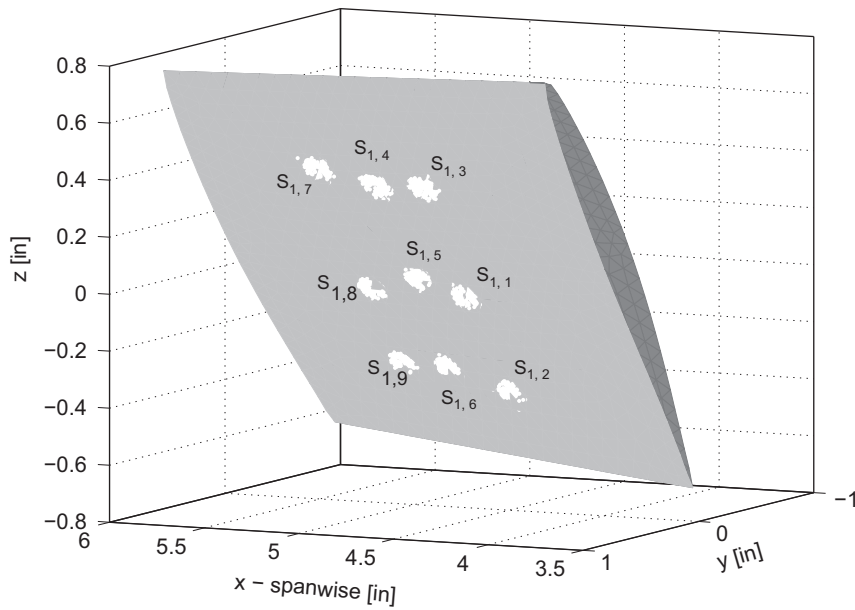
Fig. 15. Realization of the position $S_{1,p}$ ($p = 1, \ldots, 9$) of sensor S_1 on the blade's pressure surface.
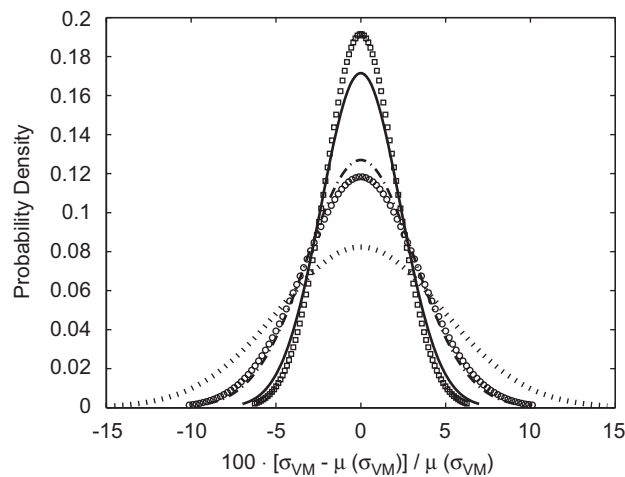

Fig. 16. Variability in maximum-stress estimate at location $S_{1,p}$ ($p = 1, 2, 5, 6, 8$) of sensor S_1 ($\omega_{1,0} = 1071.9$ Hz): — $p = 1$; □ $p = 2$; — · — $p = 5$; ○ $p = 6$; and ... $p = 8$.

and lower variance for the estimated quantity. This was not always the observed trend, as other cases instead showed an increase both in bias and spread of the estimated quantities. An example of such a situation is illustrated in Figs. 20 and 21 for the double mode at natural frequency 3366.4 Hz.

In order to assess the effect of modeling uncertainty in a more exhaustive manner, mode perturbation, which encompasses the discrepancy between numerical model and physical system, should be treated in a statistical way. As an example, as suggested by Eqs. (7), random sets of weights could be considered and propagated in a controlled simulated environment so as to isolate modeling uncertainty from other sources of error. An additional margin could then be assigned to account for interaction effects with other sources of uncertainty which would appear in a real test environment.
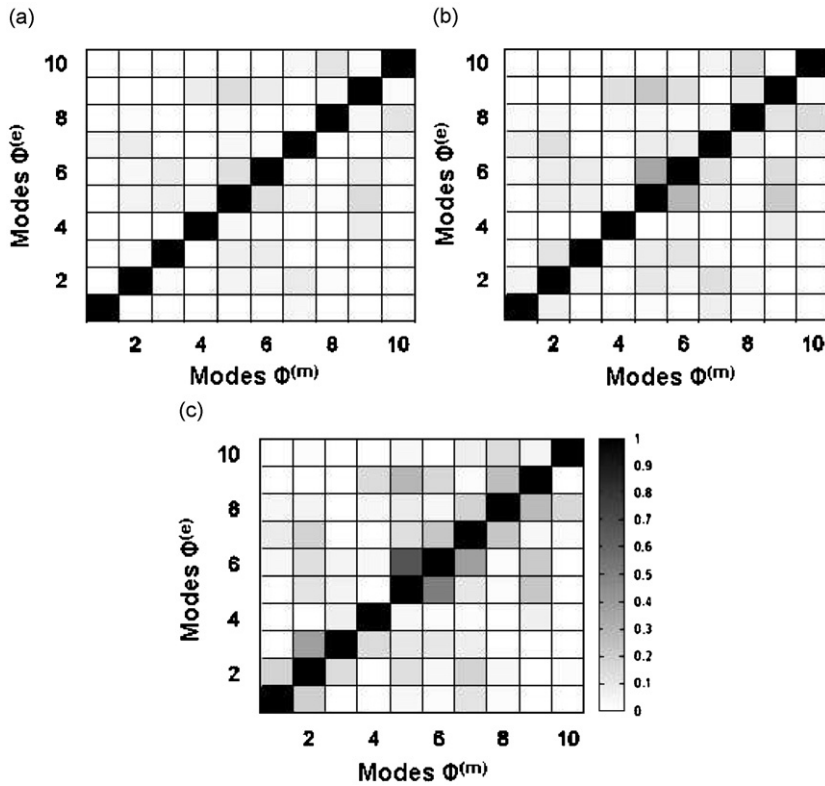
Fig. 17. MAC configurations ($\tau = 10$): (a) configuration 1 ($w_{-1} = 0$, $w_0 = 1$, $w_1 = 0$); (b) configuration 2 ($w_{-1} = 0.075$, $w_0 = 0.85$, $w_1 = 0.075$); and (c) configuration 3 ($w_{-1} = 0.15$, $w_0 = 0.70$, $w_1 = 0.15$).
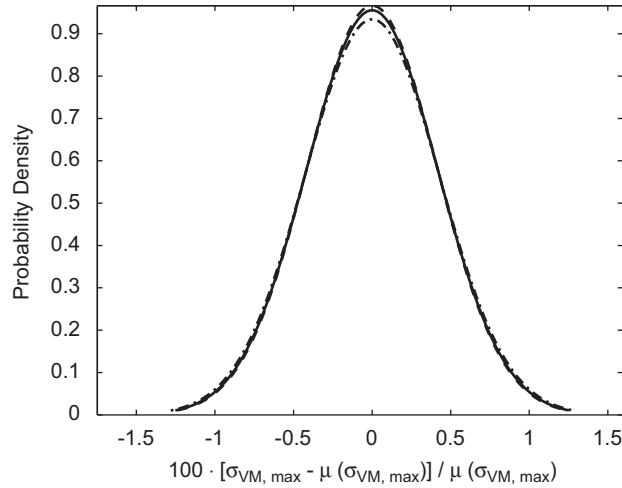

Fig. 18. Variability in maximum-stress estimate at different MAC configurations ($\omega_{1,1} = \omega_{2,1} = 839.37\,\text{Hz}$): — MAC configuration 1; – – MAC configuration 2; and —·— MAC configuration 3.

6. Conclusions

The objective of this study is to investigate a model-based estimation scheme for the prediction of a system's behavior, to assess how its accuracy is affected by the inevitable presence of uncertainties, and to quantify
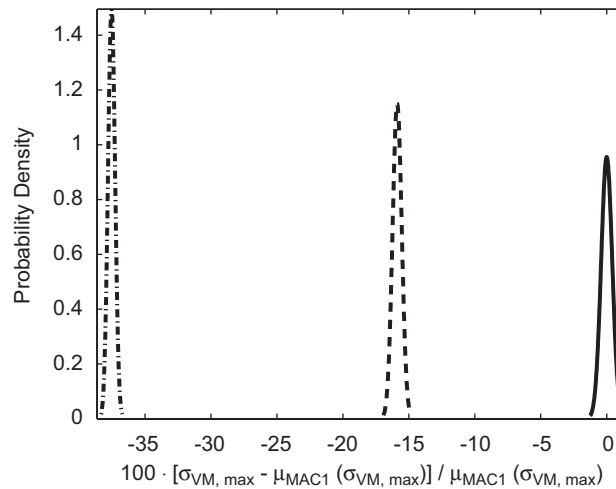
Fig. 19. Variability in maximum-stress estimate at different MAC configurations ($\omega_{1,1} = \omega_{2,1} = 839.37$ Hz): — MAC configuration 1; – – MAC configuration 2; and —·— MAC configuration 3.
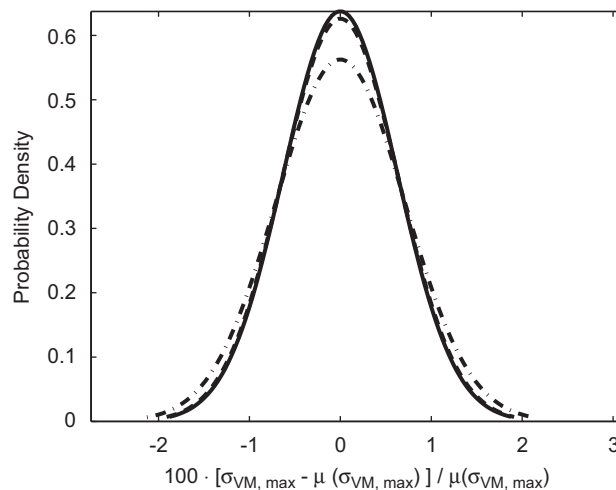

Fig. 20. Variability in maximum-stress estimate at different MAC configurations ($\omega_{3,6} = \omega_{4,6} = 3366.4$ Hz): — MAC configuration 1; – – MAC configuration 2; and —·— MAC configuration 3.

their impact in terms of confidence loss for the estimated vibratory response. Among the several classes of uncertainty that can be identified, attention was herein given primarily to instrumentation-based and system model inaccuracies, through variation of sensor locations, measurement data, and mode shapes. Uncertainties have been modeled by randomly perturbing the nominal values of given quantities (e.g., test data or model input parameters) and their impact has been investigated through a probabilistic analysis via Monte Carlo simulations. The response estimation procedure was first tried on the simple beam-like blade system to gain some insight on how uncertainties propagate and interact. The same methodology was then applied to the more complex compressor bladed disk. Similar trends were observed for both systems. On the one hand, the presence of sensor-based uncertainties highlighted the fact that an instrument's location may affect the accuracy and confidence level of a given response estimate, both explicitly and implicitly. In fact, in the presence of measurement errors only, the difference in the estimates' variability is similar to the one observed in the case of sensor location uncertainty; such a trend can then be assumed to originate from the locations at which responses are measured. Of course, a more complex system geometry and the presence of double mode
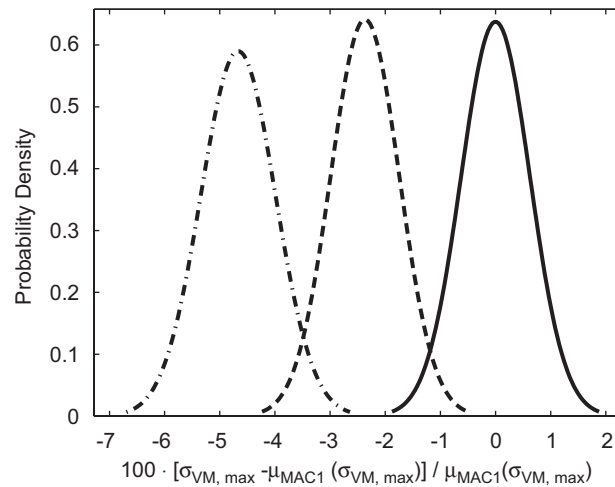
Fig. 21. Variability in maximum-stress estimate at different MAC configurations ($\omega_{3,6} = \omega_{4,6} = 3366.4\,\text{Hz}$): — MAC configuration 1; – – MAC configuration 2; and —·— MAC configuration 3.

shapes make it more difficult to anticipate how uncertainty and inaccuracies propagate within the estimation process. On the other hand, a system's model limitations and its underlying assumptions constitute another source of uncertainty, as the model itself may be incapable of describing the real component in a complete and exhaustive fashion. According to the results obtained, an increasing mismatch between the physical system's observed behavior and its numerical representation contributes to the amplification of the impact for any other source of uncertainty already affecting the accuracy of the response inference. More specifically, a growing modeling uncertainty was observed to cause an increase in the estimate's bias and spread, or simply an increase in bias accompanied by a counterintuitive shrinking of its spread. Overall, modeling uncertainties result in a further lessening of the confidence level associated with the response estimates. At this stage, only a limited set of uncertainties have been taken into consideration. Several other sources need to be addressed, such as boundary conditions, geometric localized defects, material imperfections, unknown operating conditions and applied loads, as well as noise inherent in the instrumentation (e.g., gage calibration, temperature and pressure sensitivity, nonlinearities, bandwidth error or others). Future work in this study will include the use of real measurement data obtained through experiments on physical components, and the development of an adaptive comprehensive statistical methodology capable of isolating each uncertainty source, and integrating newly available information so as to update the inferred response and improve its accuracy.

Finally, the paper has focused exclusively on direct uncertainty propagation, where certain assumptions had to be made on the statistical nature of the quantities being input in the process. The new scheme should allow for multi-directional propagation to account for interdependencies and to allow for the update/revision of those initial assumptions. To this end, the use of Bayesian networks will be investigated.

Acknowledgment

References

[1] K.L. Nichol, M.D. Sensmeier, T.F. Tibbals, Assessment of turbine engine structural integrity using the structural dynamic response analysis code (SDRAC), *Proceedings of the ASME International Gas Turbine and Aeroengine Congress and Exhibition*, Indianapolis, IN, USA, 1999.

[2] R. Rebba, S. Mahadevan, S. Huang, Inclusion of uncertainty quantification in model verification and validation, *Proceedings of Foundations '04: A Workshop for V&V in the 21st Century*, Arizona State University, Tempe, AZ, USA, 2004.

[3] J. Brown, J. Slater, R. Grandhi, Probabilistic analysis of geometric uncertainty effects on blade modal response, *Proceedings of the ASME Turbo Expo 2003 Conference*, Atlanta, GA, USA, 2003, pp. 247–255.

[4] J.H. Griffin, T.M. Hoosac, Model development and statistical investigation of turbine blade mistuning, *ASME Journal of Vibration, Acoustics, Stress and Reliability in Design* 106 (2) (1984) 204–211.

[5] M. Castanier, C. Pierre, Using intentional mistuning in the design of turbomachinery rotors, *AIAA Journal* 40 (10) (2002) 2077–2086.

[6] R. Bladh, M. Castanier, C. Pierre, Reduced order modeling and vibration analysis of mistuned bladed disk assemblies with shrouds, *Journal of Engineering for Gas Turbines and Power* 121 (3) (1999) 515–522.

[7] E. Seinturier, et al., Turbine mistuned forced response prediction comparison with experimental results, *Proceedings of the ASME Turbo Expo 2002 Conference*, Amsterdam, The Netherlands, 2002, pp. 943–952.

[8] E. Capiez-Lernout, C. Soize, J. Lombard, Blade manufacturing tolerances definition for a mistuned industrial bladed disk, *Proceedings of the ASME Turbo Expo 2004 Conference*, Vienna, Austria, 2004, pp. 307–316.

[9] A. Sinha, Computation of the maximum amplitude of a mistuned disk assembly via infinity norm, American Society of Mechanical Engineers, Aerospace Division (Publication) AD, *Analysis and Design Issues for Modern Aerospace Vehicles* 55 (1997) 427–432.

[10] A. Sinha, Computation of the statistics of forced response of a mistuned bladed disk assembly via polynomial chaos, *Proceedings of the ASME Turbo Expo 2003 Conference*, Atlanta, GA, USA, 2003, pp. 287–297.

[11] A. Sinha, Statistics of the peak maximum amplitude of the forced response of a mistuned bladed disk, *Proceedings of the ASME Turbo Expo 2005 Conference*, Reno-Tahoe, NV, USA, 2005, pp. 563–570.

[12] T.F. Tibbals, M.D. Sensmeier, K.L. Nichol, A. Stoner, C. Biegl, Model integrated testing for durability assessment of turbine engines, *Proceedings of ITEA Testing and Evaluation and Science and Technology: Forging Partnerships for the Future of Aerospace Workshop*, University of Tennessee Space Institute, Tullahoma, TN, USA, 1999.

[13] R.J. Allemang, D.L. Brown, A correlation coefficient for modal vector analysis, *Proceedings of the First International Modal Analysis Conference and Exhibit*, Orlando, FL, USA, 1982, pp. 110–116.

[14] L. Meirovitch, *Analytical Methods in Vibrations*, Macmillan, New York, NY, USA, 1967.

[15] S. Arnold, New techniques to quantify HCF margins demonstrated during accelerated mission testing, *Proceedings of 39th AIAA Joint Propulsion Conference and Exhibit*, Huntsville, AL, USA, 2003.

[16] K. Nichol, Numerical strain gage representation, *Proceedings of 39th AIAA/ASME/ASCE/AHS/ASC Structures, Structural Dynamics, and Materials Conference and Exhibit*, Long Beach, CA, USA, 1998, pp. 198–203.

[17] M.D. Sensmeier, K.L. Nichol, Optimum placement of sensors for vibration measurements on turbine engine blades, *Proceedings of 39th AIAA/ASME/ASCE/AHS/ASC Structures, Structural Dynamics, and Materials Conference and Exhibit*, Long Beach, CA, USA, 1998, pp. 1315–1320.

[18] A.J. Sanders, S. Fleeter, Experimental investigation of rotor-inlet guide vane interactions in transonic axial-flow compressor, *Journal of Propulsion and Power* 16 (3) (2000) 421–430.

[19] M. Petyt, *Introduction to Finite Element Vibration Analysis*, Cambridge University Press, Cambridge, UK, 1990.

[20] R.H. MacNeal, R.L. Harder, J.B. Mason, *NASTRAN cyclic symmetry capability*, NASTRAN: Users' Exper., MSC. Software Corporation, NASA TM X-2893, September 1973.

[21] ANSYS® Inc., *Theory Reference. ANSYS Release 10.0.*, SAS IP, Inc., © 2005.